ARTICLE

Moiré Phonons in Twisted Bilayer MoS₂

Miao-Ling Lin,[†,‡,⊥] Qing-Hai Tan,[†,‡,⊥] Jiang-Bin Wu,[†] Xiao-Shuang Chen,[¶] Jin-Huan Wang,[§] Yu-Hao Pan,[∥] Xin Zhang,[†] Xin Cong,[†,‡] Jun Zhang,[†,‡] Wei Ji,[∥] Ping-An Hu,[¶] Kai-Hui Liu,[§] and Ping-Heng Tan*[,†,‡]

[†]State Key Laboratory of Superlattices and Microstructures, Institute of Semiconductors, Chinese Academy of Sciences, Beijing 100083, China

[‡]CAS Center of Excellence in Topological Quantum Computation and College of Materials Science and Opto-Electronic Technology, University of Chinese Academy of Sciences, Beijing 100049, China

[¶]School of Materials Science and Engineering, MOE Key Laboratory of Micro-Systems and Micro-Structures Manufacturing, Harbin Institute of Technology, Harbin 150080, China

[§]State Key Laboratory of Mesoscopic Physics, School of Physics and Collaborative Innovation Center Quantum Matter, Peking University, Beijing 100871, China

[∥]Department of Physics, Renmin University of China, Beijing 100872, China

ⓢ *Supporting Information*
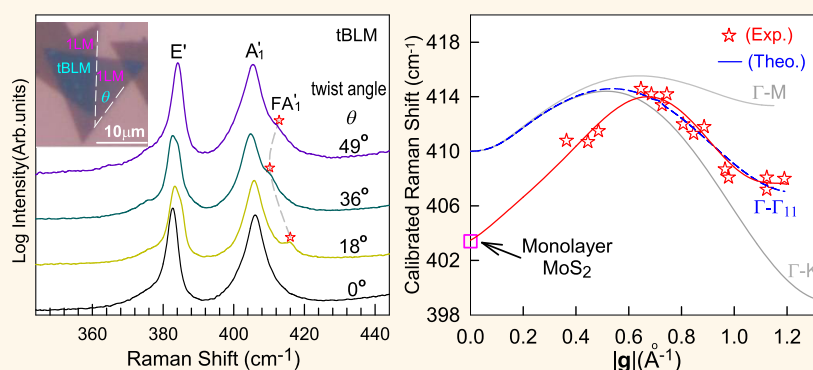
ABSTRACT: The material choice, layer thickness, and twist angle widely enrich the family of van der Waals heterostructures (vdWHs), providing multiple degrees of freedom to engineer their optical and electronic properties. The moiré patterns in vdWHs create a periodic potential for electrons and excitons to yield many interesting phenomena, such as Hofstadter butterfly spectrum and moiré excitons. Here, in the as-grown/transferred twisted bilayer MoS₂ (tBLMs), one of the simplest prototypes of vdWHs, we show that the periodic potentials of moiré patterns also modify the properties of phonons of its monolayer MoS₂ constituent to generate Raman modes related to moiré phonons. These Raman modes correspond to zone-center phonons in tBLMs, which are folded from the off-center phonons in monolayer MoS₂. However, the folded phonons related to crystallographic superlattices are not observed in the Raman spectra. By varying the twist angle, the moiré phonons of tBLM can be exploited to map the phonon dispersions of the monolayer constituent. The lattice dynamics of the moiré phonons are modulated by the patterned interlayer coupling resulting from periodic potential of moiré patterns, as confirmed by density functional theory calculations. The Raman intensity related to moiré phonons in all tBLMs are strongly enhanced when the excitation energy approaches the C exciton energy. This study can be extended to various vdWHs to deeply understand their Raman spectra, moiré phonons, lattice dynamics, excitonic effects, and interlayer coupling.

KEYWORDS: *twisted bilayer MoS₂, moiré phonons, phonon dispersion, interlayer coupling, lattice dynamics, exciton*

Compared to conventional semiconductor heterostructures, van der Waals heterostructures (vdWHs) based on two-dimensional materials (2DMs) are readily fabricated by direct chemical vapor deposition (CVD) growth[1,2] or wet/dry transfer.[3−5] These vdWHs have ultraclean and atomically sharp interfaces, providing a versatile platform for studying interface-related properties.[6−8] Also, the material

choice of the components, layer thickness, and interlayer twist angle θ widely enrich the family of vdWHs and provide multiple
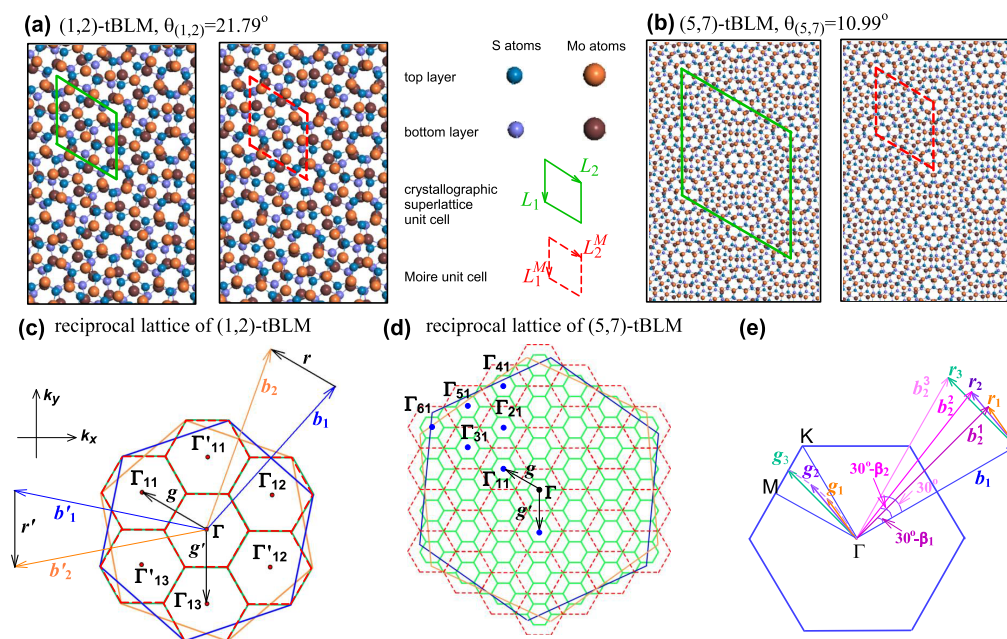
Figure 1. Crystallographic superlattice and moiré pattern in (a) (1,2)-tBLM with $\theta = 21.79°$ and in (b) (5,7)-tBLM with $\theta = 10.99°$. Dashed (red) and solid (green) parallelogram corresponds to the moiré unit cell and crystallographic superlattice unit cell of the tBLMs, respectively. The reciprocal lattice of (c) (1,2)-, and (d) (5,7)-tBLMs. The large blue and orange hexagons are the first BZ of top and bottom MoS_2 layers, and the dashed (red) and solid (green) hexagons represent the Wigner-Seitz cells of the reciprocal lattices corresponding to the moiré and crystallographic superlattices, respectively. (e) Schematic diagram of moiré basic vectors (g_i, $i = 1, 2, 3$) when $\theta \leq 30°$.

degrees of freedom to engineer their optical and electronic properties.[4,9−14] The vdWHs of transition metal dichalcogenides (TMDs) are particularly exciting for optoelectronic and light-harvesting applications,[14,15] because many monolayer TMDs are direct-bandgap semiconductors with remarkably strong light−matter interactions.[16,17] In the vdWHs, the two constituents with nearly the same lattice constant are overlaid with a relative twist angle of θ, leading to the generation of moiré patterns.[9,18−24] The moiré patterns in vdWHs will create a periodic potential based on the patterned interlayer interactions, which can impose modulation on the electronic structures of the constituent, for example, giving rise to the moiré bands in twisted bilayer graphene (tBLG) with a result that the two layers coupled strongly and Dirac velocity crosses zero several times with the twist angle reduced.[20] This periodic moiré potential can also dramatically modify the electron−electron interaction of its constituents, yielding a variety of fascinating physical behaviors. For example, direct interlayer hybridization induces van Hove singularities in tBLG, and a Hofstadter butterfly spectrum and mini-Dirac cones were observed in graphene/hBN bilayers.[9,24−28] The interlayer excitonic states in TMD-based vdWHs also experience a moiré-patterned potential, and the so-called moiré excitons exhibit signatures of the moiré pattern in the optical properties.[29]

The formation of vdWHs also affects phonons,[30−34] electron−phonon coupling (EPC),[35] and phonon−phonon interactions[36] in the constituents and the vdWH itself. Exploiting their lattice dynamics and properties of phonons enables pathways to control EPC and quantum behaviors in vdWHs. For example, the optically silent hBN phonons emerge in Raman spectra with strong intensities through resonant coupling to the electronic transitions of the WSe_2 constituent via interlayer EPC in WSe_2/hBN;[37,38] intralayer/interlayer EPC can be probed by Raman spectra of tBLG and graphene/hBN;[35] the shear (S) modes in the constituents of twisted multilayer

graphenes can be probed by resonant Raman scattering with their optically allowed electronic transitions.[39] In the MoS_2/graphene vdWHs, the S modes from the MoS_2 constituents and the layer-breathing (LB) modes from the whole vdWHs can be observed, insensitive to θ at the interface.[40]

The twisted bilayer 2DMs (tBL) can be formed when the two identical monolayers are stacked with a relative twist angle of θ. In contrast to vdWHs formed by two different 2DMs, the lattice structure of the tBL can be commensurable, such that the tBL forms a crystallographic superlattice whose superlattice period is determined by θ.[41] Therefore, a serial of folded optical and acoustic phonons should be observed in the Raman spectra of the tBL because of the phonon folding effect by the crystallographic superlattice, as reported by previous works on various superlattices.[42−45] Additionally, moiré patterns of tBLs can also introduce a periodic potential acting on the interlayer coupling between two monolayers of the tBL, which results in the formation of a moiré superlattice. The period of moiré superlattice can be equal to or smaller than that of the crytallographic superlattice in the tBL. The periodic potential induced by moiré patterns should modify the lattice dynamics of monolayer constituents to generate additional phonons in tBLs. Similar to the moiré bands[20] and moiré excitons,[29] these additional phonons modulated by the moiré patterns in tBLs can be referred as moiré phonons. Twisted bilayer TMD is one of the simplest prototypes to reveal the fundamental properties of vdWHs. For example, the interlayer coupling of twisted bilayer TMD depends on θ[46] and modifies the S and LB modes.[47,48] However, the expected moiré phonons and crystallographic-superlattice related phonons have not been observed in the Raman spectra of twisted bilayer TMD. It is not clear which kinds of phonons are dominant in the Raman spectra of twisted bilayer TMD.

Here, we use the twisted bilayer MoS_2 (tBLMs) obtained by CVD growth or precise transfer techniques as a model system to

investigate the expected moiré phonons and crystallographic-superlattice related phonons in twisted bilayer TMDs. The θ-dependent Raman modes are observed in tBLMs, which are assigned to Raman scattering of moiré phonons, rather than that of crystallographic-superlattice related phonons. Due to the weak vdW interlayer coupling between two monolayers, the phonon dispersion of monolayer MoS_2 (1LM) has been mapped by the θ-dependent frequency of moiré phonons in tBLMs, which are in line with the theoretical results by DFT calculations. Furthermore, the patterned interlayer interactions are imprints on the lattice dynamics of the moiré phonons by local atomic registries. The observations of Raman modes related to moiré phonons in tBLMs can be attributed to the resonance Raman effect with the C exciton.

RESULTS AND DISCUSSION

To discuss the possible phonon folding effects in the tBLM, we need to first analyze its crystallographic and moiré superlattices. The lattice structure of tBLM can be rigorously periodic to form the crystallographic superlattice, where the superlattice vectors of the two monolayer constituents match with each other, giving a finite unit cell. The lattice structure of the crystallographic superlattice can be represented by a pair of mutual prime numbers $(m,n)(m \neq n)$ and denoted as (m,n)-tBLM, as shown in Figure S1a of the Supporting Information (SI). The lattice structures of the (1,2)- and (5,7)-tBLMs are shown in Figure 1a,b, while those of the (2,3)- and (5,8)-tBLMs are shown in Figure S1b,c. The unit cells of the crystallographic superlattices relative to the monolayer constituent are marked by green rhombus. The twist angle θ is given by $\cos\theta = \frac{m^2 + 4mn + n^2}{2(m^2 + mn + n^2)}$. Thus, the corresponding lattice constant can be represented by $L = |L_1| = |L_2| = \frac{a|m-n|}{2\sin(\theta/2)}$, where a is the in-plane lattice constant of the 1LM. The symmetry of D_{3h} of 1LM restricts the analysis for $0 \leq \theta \leq 60°$.[49] In addition to the crystallographic superlattices, the periodic moiré patterns are also generated in tBLMs, as depicted by red rhombus. The unit cell for the moiré pattern with lattice vectors L_1^M and L_2^M can be defined, and its lattice constant is given as $L^M = |L_1^M| = |L_2^M| = \frac{a}{2\sin(\theta/2)}$. This indicates that the moiré pattern directly results from the misalignment between the top and bottom monolayers. For any θ, a moiré superlattice can be constructed, leading to the corresponding moiré reciprocal lattice. At commensurate angles, the unit cell of the crystallographic superlattice exactly matches that of the moiré superlattice if $|m-n| = 1$, as shown in Figure 1a. However, when $|m-n| = 2$ and $|m-n| = 3$, the corresponding L^M is 1/2 and 1/3 of L,[41] as depicted in Figure 1b and Figure S1c, respectively.

In the reciprocal space, the Wigner−Seitz cells corresponding to crystallographic and moiré superlattices of the (1,2)- and (5,7)-tBLMs are shown in Figure 1c,d, respectively. In each figure, the large blue and orange hexagons correspond to the first Brillouin zones (BZs) of the top and bottom monolayers, respectively. The small green and red dash hexagons represent the Wigner-Seitz cells in reciprocal space corresponding to the crystallographic and moiré superlattices, respectively. The reciprocal lattice vectors of the top and bottom MoS_2 layers can be defined as b_1, b_1' and b_2, b_2', respectively, where the length of these four vectors are equal, $b = 4\pi/\sqrt{3}a$. The two basic vectors of moiré reciprocal lattice can be evaluated as $g = b_2 - b_1$ and $g' = b_1' - b_2'$, with an absolute value $|g| = |g'| = 2b\sin(\theta/2)$, as shown in Figure 1c and section 2 of the SI. In the case of $|m-n|$

$\neq 1$, the reciprocal lattice of the moiré superlattice is incommensurate with the first BZ of 1LM and the basic vector of moiré reciprocal space should be $|m-n|$ times as large as that of crystallographic superlattice, as shown in Figure 1d. Because the basic vector of moiré reciprocal lattice is smaller than that of 1LM, there are many lattice vectors of moiré reciprocal space in the first BZ of the monolayer constituent. Since 1LM exhibits D_{3h} symmetry, all the tBLMs exhibit D_3 symmetry with a threefold rotation axis perpendicular to the hexagon plane. There are six lattice vectors with the equal length in the moiré reciprocal lattices, for example, Γ_{1i} and Γ'_{1i} (i = 1, 2, 3) in Figure 1c for the (1,2)-tBLM. The case for other tBLMs is more complicated, and there are many sets of Γ_{ji} (i = 1, 2, 3) and Γ'_{ji}, j = 1, 2, ... from zone center to the zone edge of 1LM. For each j, there are three equivalent Γ_{ji} and three equivalent Γ'_{ji} (i = 1, 2, 3), but Γ_{ji} and Γ'_{ji} are inequivalent to each other. In Figure 1d, the sites of Γ_{j1} (j = 1, 2, ..., 6) are labeled. The length of Γ_{1i} and Γ'_{1i} is equal to $|g|$. By varying θ, the trajectory of g can be obtained, as shown by the dashed line in Figure 1e. Figure 1e shows the basic vectors of moiré reciprocal lattice, g_1, g_2, and g_3, for tBLMs with twist angles of $30° - \beta_1$, $30° - \beta_2$, and $30°$, respectively, and those for tBLMs with twist angle larger than $30°$, for example, $30° + \beta_1$ and $30° + \beta_2$, are shown in Figure S2.

It should be noted that the moiré superlattice with twist angles $30° - \beta$ and $30° + \beta$ are two commensurate partners, whose supercells have the same lattice constant in a primitive cell. For example, the (1,4)-tBLM with twist angle, $\theta_{(1,4)} = 38.21°$, is the commensurate partner of that with $\theta_{(1,2)} = 21.79°$, as shown in Figure S3. In addition, the basic vectors of moiré reciprocal lattices of the two commensurate partners with the twist angle $30° - \beta$ and $30° + \beta$ are mirror symmetrical to each other with regard to the $\Gamma−K'$ axis, as depicted in Figure S4. Since the 1LM belongs to the D_{3h} symmetry, the basic vectors of moiré reciprocal lattices of these two commensurate partners are equivalent to each other.

In the tBLs, the moiré patterns can introduce periodic potentials on each constituent and form moiré superlattices. Indeed, in the tBLGs and tBLMs, such periodic modulation on the interlayer interactions makes the in-plane displacement of the two layers not produce any overall restoring force so that the shear frequency is almost zero and therefore not detected.[39,47,48,50] Because the interlayer interaction in the tBLs is not strong enough to form a lattice-matched coherent structure, the moiré potentials introduce a perturbation into the phonon modes of the two constituents. Thus, the phonons in the BZ interior of the monolayer constituent linked with the lattice vectors Γ_{ji} and Γ'_{ji} of the moiré reciprocal space can be folded onto the zone center Γ, and these phonons may become Raman active in the tBLs. Furthermore, a crystallographic superlattice can be naturally formed in tBLs, which induces a smaller reciprocal unit cell in tBLs relative to that of the monolayer constituent. The formation of the superlattice will not significantly modify the phonon frequency of the monolayer constituent too. Therefore, some zone-center phonons of tBLs can be folded from the off-center phonons of the monolayer constituent linked with the reciprocal lattice vectors of the crystallographic superlattice. These zone-center phonons may also become Raman active in tBLs. In contrast to monolayer constituent, more Raman modes are expected to be observed in tBLs no matter whether the folded phonons are from crystallographic superlattices or moiré superlattices. Therefore, the detailed Raman experiments on the tBLs should be done to clarify this effect.
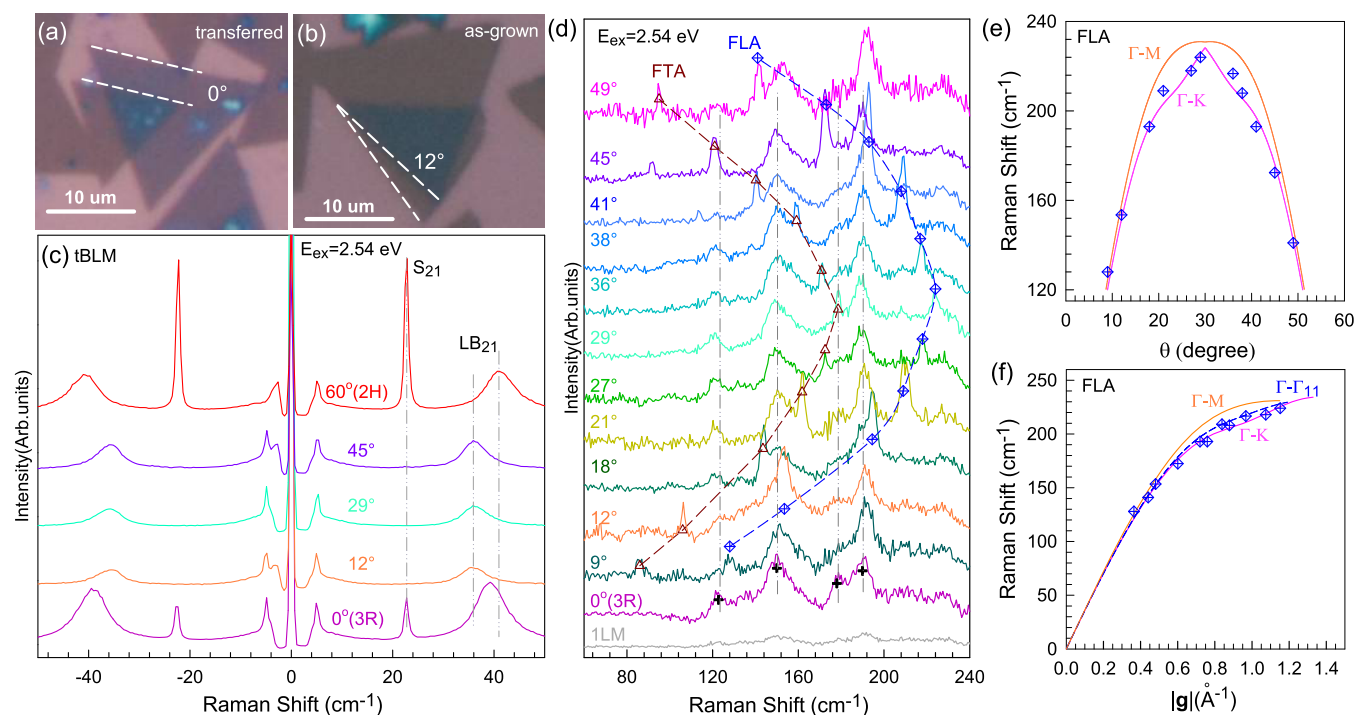
Figure 2. Optical images of the tBLM samples with twist angles of θ = (a) 0° and (b) 12°. The sample in (a) is produced by transferring a CVD-grown 1LM onto another one, while that in (b) is produced by direct CVD synthesis. (c) The Raman spectra of 3R- and 2H-BLMs and other tBLMs in the ultralow-frequency region, E_{ex} = 2.54 eV. The vertical dashed lines are guides to eyes. (d) Raman spectra of tBLMs with different θ and 1LM in the region of 60−240 cm^{-1} under 2.54 eV excitation. The dark red and blue dashed lines are guides to eyes to represent the two series of Raman modes with θ-dependent frequencies. The vertical dash-dotted lines correspond to the peak positions of the second-order Raman modes. The (e) θ- and (f) $|g|$-dependent frequencies of the FLA modes, where $|g|$ is the basic vector of moiré reciprocal lattice. The θ-dependent LA phonon frequencies along the Γ−K (pink) and Γ−M (orange) directions are also plotted in (e), where the relations between wave vector and θ are $|g| = 2b\sin(\theta/2)$ if 0° < θ < 30° and $|g| = 2b\sin((60-\theta)/2)$ if 30° < θ < 60°. The blue dashed line in (f) is the phonon dispersion of LA phonon branch along g. The crossed diamonds represent the experimental Pos(FLA) of tBLMs. The LA phonon dispersions along Γ−K (pink) and Γ−M (orange) directions are also plotted.

We measured Raman spectra of tBLMs produced by transferring one piece of CVD-grown 1LM onto another one or by direct CVD synthesis. The typical optical images of the transferred and as-grown tBLMs with different θ are depicted in Figure 2a,b, respectively. Because the grain-boundary formation is driven by growing kinetics of MoS$_2$, the single crystalline MoS$_2$ tends to form an equilateral triangle with specific atomic arrangements at the edge.[51−53] Therefore, the twist angle of the tBLMs can be determined by the relative directions of triangle edges,[46] as shown in Figure 2a,b. It had shown that the LB mode of two-dimensional vdWHs provides a direct evidence for the good interfacial coupling between the constituents,[40] therefore, we first checked the S and LB modes of tBLM under 2.54 eV excitation to confirm the good interfacial coupling of the transferred and as-grown tBLMs in this study, as shown in Figure 2c. The 2H stacking at θ = 60° and 3R stacking at θ = 0° are the first and second most stable stacking for bilayer MoS$_2$ (BLM), and thus tBLMs tend to exhibit 3R and 2H stacking when its twist angle is θ = 0° and θ = 60°, respectively. It was predicted that the S mode, S$_{21}$, of 3R-stacked BLM (3R-BLM) should be at the same peak position as that of 2H-stacked BLM (2H-BLM) but exhibit weaker Raman intensity relative to the LB mode compared with that of 2H-BLM,[47] which had been considered as a pathway to distinguish the 3R from 2H stacking. Indeed, Figure 2c shows that the S$_{21}$ mode in the tBLM with θ = 0° exhibits weaker intensity relative to the corresponding LB mode and identical peak frequency with respect to that in the tBLM with θ = 60°. Therefore, the tBLMs with θ = 0° and θ = 60° in

this study are in 3R and 2H stacking, respectively. The absence of the S$_{21}$ modes in all the tBLMs with 0° < θ < 60° suggests that the interlayer shear coupling is not enough to produce an overall restoring force between the two monolayer constituents, in good agreement with the previous studies.[47,48] The modes, LB$_{21}$, emerge in the Raman spectra of all the BLMs. For each transferred tBLM studied in this work, the frequency of the LB mode is very uniform in the whole tBLM area, which indicates the uniformity of the interfacial coupling for the transferred tBLMs. This had also been confirmed by the case of BLM/graphene heterostructures.[40] The peak position of LB$_{21}$ mode (Pos(LB$_{21}$)) of 3R-BLM ($\sim$39 cm^{-1}) is smaller than that of 2H-BLM ($\sim$41 cm^{-1}), which is in line with the previous theoretical results.[47] This further confirms our assignments of 3R and 2H stacking for tBLMs with θ = 0° and θ = 60°. Furthermore, the LB$_{21}$ modes of all the tBLMs with 0° < θ < 60° are located at the same position ($\sim$36 cm^{-1}) and slightly smaller than that of 2H-BLM, no matter if they are produced by the direct CVD synthesis or wet transfer. This indicates that the interfacial LB couplings between the two monolayer constituents of all the tBLMs are comparable with that of 2H-BLM, which is essential for the formation of the moiré patterns and crystallographic superlattice in all the tBLMs to observe the corresponding folded phonons.

Figure 2d shows the Raman spectra in the region of 60 to 240 cm^{-1} of the tBLMs with θ ranging from 9° to 49° under the excitation energy E_{ex} = 2.54 eV. In contrast to 1LM, the Raman modes associated with the second-order Raman scattering of the
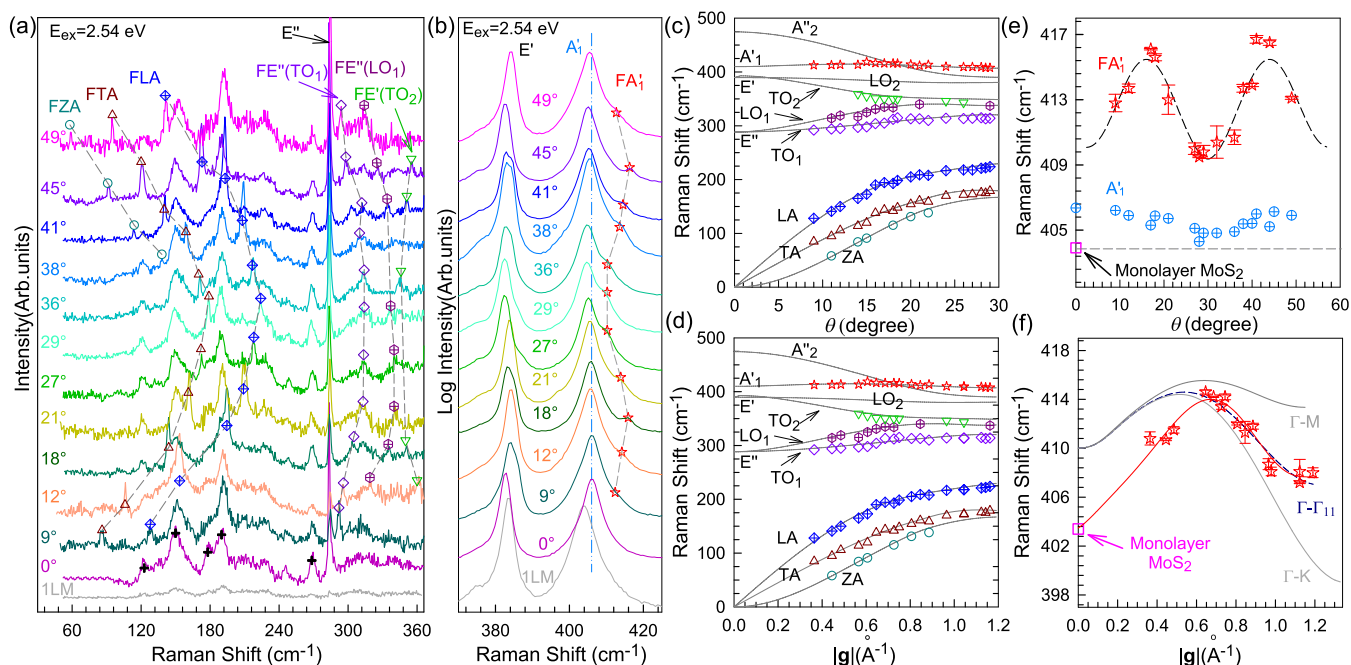
Figure 3. Raman spectra of tBLMs in the region of (a) $50-365$ cm^{-1} and (b) $370-425$ cm^{-1}. Different shapes and color symbols represent the Raman modes in different phonon branches. The Raman spectra of 1LM and 3R-BLM ($\theta = 0°$) are plotted for comparison. (c, d) The comparison of calculated and experimental frequencies of moiré phonons dependent on θ (c) and $|g|$ (d). The solid gray lines are the calculated phonon frequencies by the interpolation between those along the $\Gamma-M$ and $\Gamma-K$ directions in 1LM, and the scatter symbols are the experimental results. (e) θ- and (f) $|g|$-dependent frequencies of FA_1' mode. The error bars of Pos(FA_1') are also shown. The Pos(A_1') of the 3R-BLM and other tBLMs (crossed circles) and 1LM (pink square) are also summarized in (e). The theoretical phonon dispersion of the A_1' mode in 1LM along the $\Gamma-K$ and $\Gamma-M$ directions (gray) are also plotted in (f). The dashed line is the phonon dispersion of the A_1'-related branch along g in 1LM. The stars represent the experimental Pos(FA_1') in tBLMs with θ ranging from 0° to 60°.

longitudinal acoustic (LA), transverse acoustic (TA), out-of-plane acoustic (ZA), longitudinal optical (LO), and transverse optical (TO) phonons at K and M points of BZ were observed in the Raman spectra of 3R-BLM ($\theta = 0°$), which can be assigned as the second-order Raman modes, $A_1'(M)$-$E''(M)^{TO_1}$ (~ 120 cm^{-1}), $E'(M)^{LO_2}$-LA(M) (~ 150 cm^{-1}), $A_1'(M)$-LA(M) (~ 178 cm^{-1}), and TA(K) (~ 190 cm^{-1}).[54,55] These modes have been observed in other tBLMs, independent of θ, as indicated by the vertical dash-dotted lines. Apart from these second-order Raman modes, two series of θ-dependent Raman modes are also observed in both the as-grown and transferred samples, as depicted by the triangles and diamonds, respectively. In principle, these modes can be attributed to the folded phonons of 1LM due to the presence of moiré or crystallographic superlattices in the tBLMs. No matter which folding mechanism is dominant in the tBLMs, the folded phonons should be from the same physical origin. The two additional modes observed in the range of $120-240$ cm^{-1} with strong intensity for each sample are in the frequency region of LA and TA branches of 1LM. Therefore, these two additional Raman modes can be attributed to folded LA (FLA) and folded TA (FTA) phonons of 1LM. The peak positions of the FLA modes are summarized in Figure 2e as a function of θ, showing a mirror behavior with regard to $\theta = 30°$. Notably, all the FLA modes are fitted with the same full width of half-maximum. The fitting errors in Pos(FLA) are smaller than the sizes of symbols so they are not included in Figure 2e,f. The maximum peak position of this serial of modes is located at ~ 225 cm^{-1}, close to the maximum frequency of LA phonon branch, further confirming our assignment.

To figure out the physical origin of the folded phonons, we carefully check Raman spectrum of the tBLM with $\theta = 12°$,

approximate to that of the (5,7)-tBLM in Figure 1b,d. In principle, the FLA phonons with lattice vectors in reciprocal space corresponding to the moiré superlattice (Γ_{ji}, $j = 1, 2, ..., 6$; $i = 1, 2, 3$) and crystallographic superlattice (the centers of all small green hexagons) can be activated in the Raman spectra by phonon folding effect, whose frequency ranges from 70 to 230 cm^{-1} according to the length of the lattice vectors. However, only one peak (at ~ 153 cm^{-1}) from the FLA phonon is observed, which indicates that only one LA phonon is folded onto the zone center of monolayer constituent. According to the phonon dispersion of LA branch along $\Gamma-K$ direction,[56] the frequency of the FLA mode at 153 cm^{-1} corresponds to the vector of 0.49 Å^{-1}, almost equal to the basic vector of moiré reciprocal lattices ($|g|$) of 0.48 Å^{-1}. This vector is about twice in length as much as that of the basic vector in the reciprocal space of crystallographic superlattice. Therefore, the LA phonon linked with the basic vector of moiré reciprocal space is involved in the phonon folding effect of tBLMs, while that in the reciprocal space of crystallographic superlattice is not involved. The LA phonons corresponding to other lattice vectors in reciprocal space of moiré and crystallographic superlattices are also suppressed in the Raman spectra. Based on the θ-dependent basic vectors of moiré reciprocal lattices $|g| = 2b \sin(\theta/2)$, the LA dispersions along $\Gamma-K$ and $\Gamma-M$ directions can be transformed to θ-dependent LA phonon frequencies, which are plotted in Figure 2e. The experimental Pos(FLA) are in line with the θ-dependent LA phonon frequencies along $\Gamma-K$ and $\Gamma-M$ directions, especially those along $\Gamma-K$ direction. By comparing the Pos(FLA) with the phonon frequency along $\Gamma-K$ direction, the twist angle of tBLM can be estimated.

To further understand the θ-dependent Pos(FLA), we plotted the phonon dispersion of the LA phonon branch in 1LM[56] along the $\Gamma-M$ and $\Gamma-K$ directions in Figure 2f. With the relation between θ and g addressed above, the phonon dispersion of the LA-related branch along g in Figure 1e can be interpolated from the LA phonon frequencies along the $\Gamma-M$ and $\Gamma-K$ directions. The detailed demonstrations of the interpolation can be found in Figure S5. The derived g-dependent experimental Pos(FLA) is depicted in Figure 2f by the diamonds, which is in agreement with the calculated LA dispersion along the g trajectory. This further confirms that the additional observed modes are the folded LA phonons related to the basic vectors of moiré reciprocal lattices of tBLMs. Therefore, these folded phonons are actually the so-called moiré phonons. The invisibility of the phonons with other vectors in reciprocal lattices corresponding to the moiré and crystallographic superlattices may be attributed to the incommensurate twist angle or weak electron–phonon coupling. The phonon dispersion of FLA moiré phonons along the g trajectory approximates to that along $\Gamma-K$ direction in 1LM. This indicates that the phonon dispersion of the LA branch along the $\Gamma-K$ direction in monolayer constituent can be estimated by the frequencies of the corresponding moiré phonons in tBLMs.

In the tBLM, there are six moiré phonons for each phonon branch, which originate from the phonons related to six basic vectors of moiré reciprocal lattice with equal length, Γ_{1i} and Γ'_{1i} (i = 1, 2, 3) of the monolayer MoS_2 constituent, similar to those shown in Figure 1c. We define the six moiré phonons as MP(Γ_{1i}) and MP(Γ'_{1i}) (i = 1, 2, 3), respectively. If we neglect the interlayer interaction in the tBLM, the frequencies of these six moiré phonons of the LA branch should be degenerate and only one Raman mode corresponding to the FLA phonon can be observed. This is in good agreement with the Raman experiment. Thus, the observed frequency of moiré phonons in the tBLM is expected to show small deviation to that of the corresponding phonons of the monolayer constituent, providing a way to trace the corresponding phonon dispersion.

In addition to the moiré phonons related with the LA phonon branch, the Raman modes related to the moiré phonons of other phonon branches have also been observed, as shown in Figure 3a,b. We first assign the θ-independent Raman peaks in tBLMs. Considering the D_3 symmetry of the tBLM, the corresponding irreducible representation of Raman modes at the BZ center should be $\Gamma = A_1 + A_2 + E$. In order to clearly show the origins of these Raman modes, here we denote them by the irreducible representation of Raman modes at Γ in 1LM. The two prominent peaks at about 385 and 405 cm^{-1} in Figure 3b are attributed to the nonfolded E and A_1 modes. The two modes originate from the E' and A'_1 modes at Γ of the monolayer constituent, therefore, the nonfolded E and A_1 modes in the tBLM are denoted as E' and A'_1, respectively. In the region of 50−365 cm^{-1}, the Raman signals from 1LM are very weak. For the 3R-BLM ($\theta = 0°$), the E'' mode (at ∼284 cm^{-1}) and other Raman modes labeled by crosses are observed. These Raman modes are also observed in other tBLMs, whose frequency is independent of θ. The $E''(\Gamma)$ mode is related to the degenerate LO and TO phonons at zone center, which is Raman active but not present in 1LM in the back-scattering configuration. Its observation in tBLMs can be attributed to the lower symmetry in comparison with 1LM. Besides the second-order Raman modes assigned above, the peak at ∼268 cm^{-1} can be assigned as the second-order Raman modes of $A'_1(M)$-TA(M).[55]

In the region of 50−365 cm^{-1}, the six series of θ-dependent Raman peaks are observed in total in the tBLMs. In addition, a weak θ-dependent peak is observed around 410 cm^{-1} as a shoulder on the high-energy side of each A'_1 peak. The θ- and g-dependent phonon frequencies of all the additional observed modes are summarized in Figure 3c,d, respectively. The phonon dispersion curves of 1LM along g are also included in Figure 3d, which are interpolated from the theoretical ones of 1LM along the $\Gamma-M$ and $\Gamma-K$ directions.[56] The theory−experiment comparison indicates that from low to high frequency, the seven series of θ-dependent Raman modes are identified as Raman scattering from moiré phonons associated with ZA, TA, LA, $E''(TO_1)$, $E''(LO_1)$, $E'(TO_2)$ and A'_1 branches in 1LM, respectively. They are *folded* onto the zone center and become Raman active. Accordingly, the corresponding Raman modes can be assigned as FZA, FTA, FLA, $FE''(TO_1)$, $FE''(LO_1)$, $FE'(TO_2)$ and FA'_1, respectively, by using symmetry denotation of 1LM. All these moiré phonons exhibit a mirror behavior with regard to $\theta = 30°$, similar to the FLA peaks. It should be noted that the Raman modes related to these moiré phonons share several common features, such as the weak intensity, narrow line width, and θ-dependent frequency. Therefore, it is easy to distinguish the Raman modes associated with the moiré phonons from other phonon modes. The good agreement between experimental frequencies of moiré phonons and theoretical dispersion curves traced by the basic vectors of moiré reciprocal lattice indicates that the moiré phonons can serve as a fingerprint to determine θ of the tBLMs.

Pos(A'_1) in the tBLM was found to be sensitive to its θ.[46] The observation of the FA'_1 mode makes it possible to probe the phonon dispersion of the A'_1-related branch. We summarized the θ-dependent Pos(FA'_1) and Pos(A'_1) of tBLMs in Figure 3e. The Pos(A'_1) in 1LM is also presented. Because the periodic moiré potential in tBLMs introduces a perturbation into the interlayer distance and thus a perturbation into the interlayer coupling between the two constituents,[47] Pos(A'_1) undergoes fluctuations in tBLMs with various θ, exhibiting barely a "V-shape" behavior, as shown in Figure 3e. Due to the presence of interlayer coupling in tBLMs, its Pos(A'_1) is larger than that of 1LM. If supposing that the interlayer-coupling induced frequency shift of Pos(FA'_1) is the same as that of Pos(A'_1) for the same tBLM, Pos(FA'_1) can be calibrated by the frequency difference of Pos(A'_1) between tBLMs and 1LM, and Pos(FA'_1) related with g in reciprocal lattice of 1LM can be obtained, as shown in Figure 3f along with Pos(A'_1) of 1LM at Γ. The interpolated phonon dispersion of the A'_1-related branch in 1LM along the g trajectory is also represented in the Figure 3f together with that of the A'_1-related branch along the $\Gamma-M$ and $\Gamma-K$ directions.[56] When the g vector is larger than 0.6 $Å^{-1}$, the experimental Pos(FA'_1) dependent on g is in agreement with the interpolated phonon dispersion along the g trajectory in the BZ of 1LM. However, the experimental data show deviations from the interpolated phonon dispersion along g trajectory when the vector is below ∼0.6 $Å^{-1}$. Considering the Pos(A'_1) of ∼403.4 cm^{-1}[57] is lower than the calculated frequency of phonon at Γ, the real phonon dispersion should decrease more sharply toward Γ than the interpolated phonon dispersion when it approaches $g = 0$ (Γ). Therefore, we can map the real phonon dispersions of the A'_1-related branch in the monolayer constituent from the θ-dependent Pos(FA'_1) of tBLMs, as indicated by the solid line in Figure 3f. The present experimental data show that further theoretical works should make an effort to improve the accuracy of the phonon dispersion of the A'_1-related branch close to the Γ point in 1LM.
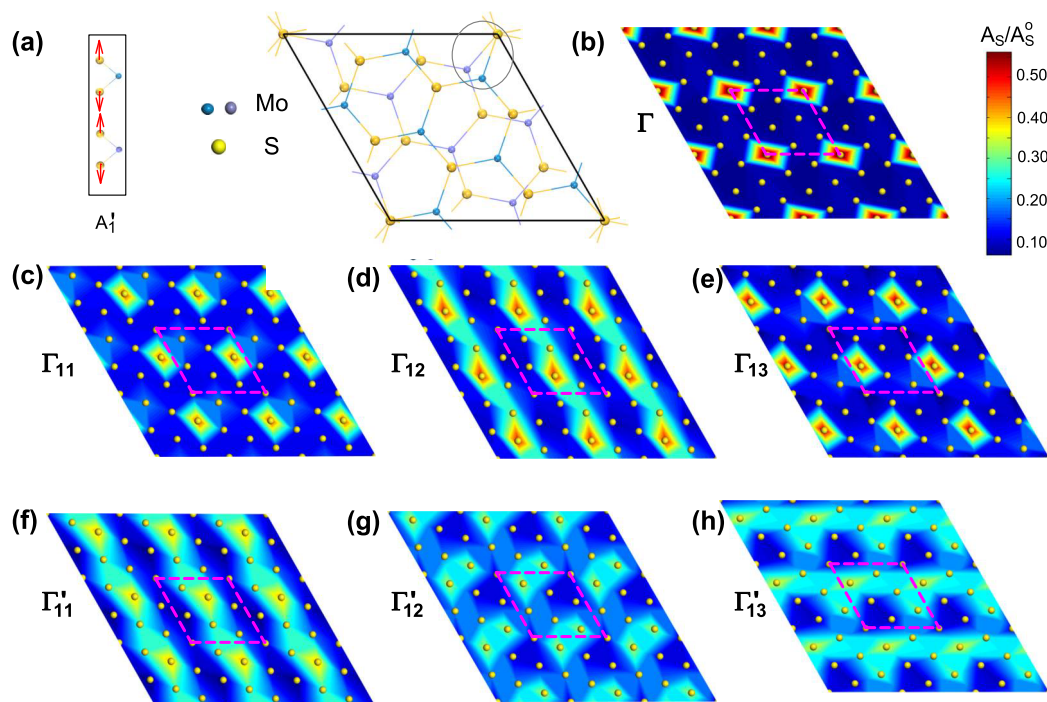
Figure 4. (a) The atom vibration of A_1' mode in AA-stacked BLM and the lattice structure of tBLM with $\theta = 21.79°$. The distribution of vibration amplitude of the topmost S atoms (A_S) of the top MoS$_2$ layer related to nonfolded A_1' modes at (b) Γ and FA_1' modes at (c) Γ_{11}, (d) Γ_{12}, (e) Γ_{13}, (f) Γ_{11}', (g) Γ_{12}', and (h) Γ_{13}' in a 3×3 supercell of the tBLM. The A_S is normalized by the vibration amplitude of the A_1' mode (A_S^0) in 1LM.
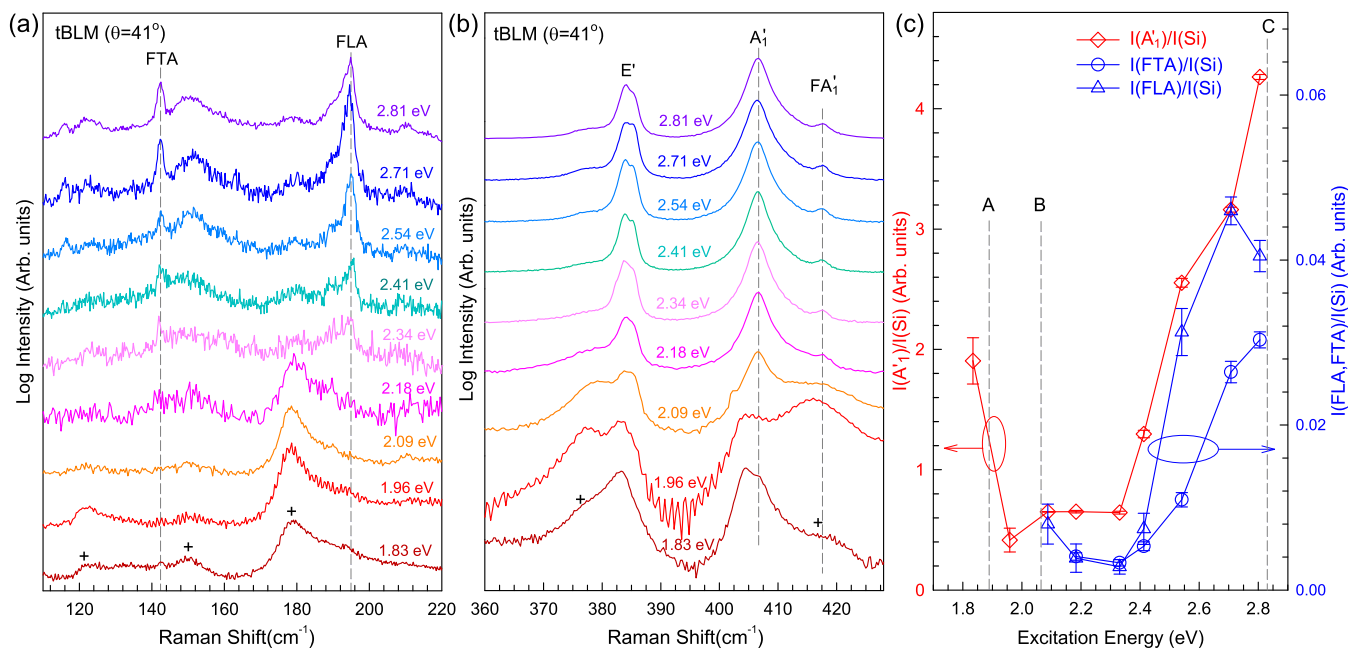

Figure 5. Raman spectra of (a) FTA, FLA, (b) E', A_1', and FA_1' modes of the tBLM with $\theta = 41°$ excited by E_{ex} from 1.83 to 2.81 eV. Each spectrum is normalized by the intensity of its A_1' mode. The crosses represent the second-order Raman modes which are also observed in the 3R-BLM ($\theta = 0°$). (c) I(FTA), I(FLA), and I(A_1') as a function of E_{ex}. The intensity of the three Raman modes is normalized by that of the Si peak at ~520 cm^{-1}. The gray vertical lines represent the energies of A, B, and C excitons in 1LM.

In tBLMs, the periodic moiré potentials induced by moiré patterns produces the locally different interlayer registry, which are expected to impose a patterned modulation onto the lattice dynamics of the moiré phonons. We employ the density functional perturbation theory (DFPT)[58] (see Methods and Experiments for details) to study the effect of the patterned interlayer interaction on the lattice dynamics, taking the FA_1'

mode in the (1,2)-tBLM as an example. Figure 4a plots the schematic diagram of atom vibrations for the A_1' mode in AA-stacked BLM and the lattice structure of the (1,2)-tBLM with $\theta_{(1,2)} = 21.79°$. Figure 4b–h shows the vibration amplitudes of the topmost S atoms (A_S) of the top MoS$_2$ layer in a 3×3 supercell for the nonfolded A_1' mode and the six FA_1' moiré phonons in the tBLM, respectively. The A_S in the tBLM is

normalized by the vibration amplitude of the topmost S atoms for the A_1' mode (A_S^0) in 1LM. As shown in Figure 4b, after twisting from the AA-stacked BLM, the atom vibration of the topmost S atoms for the nonfolded A_1' mode is localized at the four corners of the unit cell of the tBLM, while for the FA_1' moiré phonons, the amplitude of the S atoms at the four corners is quite small. The atomic vibration of $MP(\Gamma_{1i}')$ is more nonlocalized in the unit cell than that of $MP(\Gamma_{1i})$, and the vibration amplitude of $MP(\Gamma_{1i}')$ is also weaker than that of $MP(\Gamma_{1i})$. Although the frequencies of these six moiré phonons are degenerate to lead to one Raman mode, the vibration amplitude distributions of each moiré phonon are strongly modified by the local atomic environments. This implies that the moiré patterns can impose a nanometer-scale patterned interlayer interaction to modulate the lattice dynamics of the moiré phonons by local atomic registries, providing a way to manipulate the interlayer coupling in the tBLM.

In tBLGs, additional Raman modes were observed in the Raman spectra in comparison with the monolayer constituent.[30,31,35,39,59,60] Several groups reported that these Raman modes correspond to the phonons in the monolayer graphene selected by the basic vector of moiré reciprocal lattice *via* rich resonance effects. Furthermore, the LB modes linked with the basic vector of moiré reciprocal lattice were also observed in the ultralow-frequency Raman spectra.[61] In fact, based on our analysis above, these Raman modes correspond to the moiré phonons in tBLGs, which are induced by the phonon folding effect in tBLGs. The Raman intensity related to these moiré phonons exhibits significant dependence on θ due to rich resonance effects in tBLGs.[60,62,63] However, the Raman intensity of moiré phonons in the tBLM weakly depends on θ. As shown in Figure 3, the Raman modes related to the moiré phonons of all the samples with different θ are obviously observed under E_{ex} = 2.54 eV, quite different from the case in tBLGs. In order to clarify whether the resonance effect exists in the Raman scattering of moiré phonons in tBLMs, nine excitation energies in the range of 1.83−2.81 eV were applied to measure the Raman spectra of the FTA, FLA, and FA_1' modes in the tBLM with θ = 41°, as shown in Figure 5a,b, whose Raman intensity is normalized by that of A_1' $(I(A_1'))$. The resonant Raman profiles of the A_1', FTA, and FLA modes are plotted in Figure 5c, in which the intensities of all the Raman modes are normalized by the intensity of the Si peak at ~520 cm^{-1} to eliminate the effect of different efficiencies of Raman system at different E_{ex}. The FLA, FTA, A_1', and FA_1' modes excited by different E_{ex} are fitted by Lorentizian lineshapes with the fixed peak positions and line widths, respectively. When E_{ex} approaches the A (~1.89 eV) and B (~2.06 eV) excitons of 1LM, the second-order Raman peaks (the peaks marked with crosses) are significantly enhanced *via* the double resonance Raman scattering, resulting in the difficulties to distinguish the Raman modes of moiré phonons and A_1' mode from the second-order Raman peaks. This can also be depicted by the increase of fitting errors shown in Figure 5c. Thus, the resonance behaviors of the moiré phonons with the A and B excitons are beyond this study. As depicted in Figure 5b, FA_1' mode exhibits similar resonance behavior to the corresponding nonfolded A_1' mode, whose intensity is enhanced when E_{ex} matches the energy of C exciton. The FTA and FLA modes are also enhanced when E_{ex} is close to the energy of the C exciton, as shown in Figure 5c. This implies that the resonance Raman effect of moiré phonons results from the excitonic effects.[64−67] Although the Raman intensity of moiré phonons is insensitive to θ, the proper

selection of E_{ex} is needed to observe Raman scattering of moiré phonons.

As discussed above, due to the weak interlayer coupling in tBLMs, the moiré phonons can be used to map the phonon dispersions of its monolayer constitute. In general, by varying the θ, the frequencies of moiré phonons related to LA and TA phonon branches in tBLs based on 2H-TMDs approximate to the corresponding phonon dispersion along Γ−K direction in the corresponding monolayer 2H-TMDs due to the quasi isotropy of these phonon dispersions in the basal plane. Conversely, the twist angle of tBLs based on 2H-TMDs can be approximately estimated by comparing the peak positions of FLA and FTA modes with the corresponding phonon frequency along the Γ−K direction of the monolayer constituent. The detection of moiré phonons in twisted bilayer TMDs is not so critical as the case in tBLGs, and only one E_{ex} can be used to detect all the Raman modes corresponding to the moiré phonons in twisted bilayer TMDs with different θ under the resonant or near-resonant conditions. Therefore, this approach can be applied to other types of tBLs. Besides the tBLs, twisted multilayer 2DMs can also be prepared, such as twisted $(m + n)$-layer graphenes.[39,68] The moiré phonons related to each constituent should also be observed in the Raman spectra, making it possible to probe the phonon dispersion of the multilayer constituents. Furthermore, moiré superlattices can still be generated between the two constituents with nearly the same lattice constant, and thus moiré phonons are expected in these vdWHs. This study makes it possible to probe the moiré phonons in various vdWHs.

CONCLUSIONS

In conclusion, we have observed Raman modes related to moiré phonons in the as-grown/transferred tBLMs. The moiré phonons originate from the phonons in monolayer constituents with the basic vectors of moiré reciprocal lattices, which are folded onto the zone center due to the modulation of the periodic moiré potentials. Because of the weak interlayer coupling in tBLMs, the phonon dispersions of the monolayer constituent can be probed by the θ-dependent frequency of moiré phonons. In addition, the moiré patterns can impose a nanometer-scale patterned interlayer interaction, which significantly influences the lattice dynamics of moiré phonons by local atomic registries, as supported by the DFT calculation. The Raman modes of moiré phonons in the tBLMs are significantly enhanced when E_{ex} matches to the C exciton energy, showing a similar resonant profile to that of nonfolded Raman modes. Because the phonon folding effect related to moiré phonons is mastered by the basic vector of moiré reciprocal lattices, rather than by that in the reciprocal lattices of crystallographic superlattices of tBLs, this study can be extended to other tBLs and the related vdWHs.

METHODS AND EXPERIMENTS

Sample Preparation. The samples are produced by direct CVD synthesis and by wet transfer. For as-grown tBLMs, molybdenum oxide (MoO$_3$) powder (99.9%, 35 mg, Aladdin) and sulfur powder (99.95%, 0.4 g, Aladdin) were placed on different temperature zones, while the Si/SiO$_2$ substrate was placed about 2−4 cm away from the MoO$_3$ precursor in a high-temperature zone (~670°C) with a heating ramp of 15 °C/min after being cleaned. The reaction time was kept for 20−25 min under atmospheric pressure with the argon gas flow 10−20 sccm. With the enhanced gas stream (15−20 sccm), the proportion of BLM was increased. After the growth, the furnace was cooled to the room temperature. For the transferred samples, the 1LM was first produced

by CVD using similar process as described above. However, the S powder was placed at the upstream side 13 cm from the MoO_3 powder, while the SiO_2/Si substrate was placed upon the crucible containing MoO_3 powder. The CVD process was performed under ambient pressure, controlled ultrahigh-purity Argon gas. The recipe is kept at 105 °C, 500 sccm gas flow for 1 h, ramped to 775 °C with 15 sccm gas flow in 44 min, kept at 775 °C with 15 sccm gas flow for 10 min, and then naturally cooled down to room temperature. After that, the 1LM is transferred onto another piece of 1LM by wet transfer.[3] All the transferred samples were annealed after the transfer process to remove the residues from samples during transferring.

Raman Measurements. Raman spectra are measured at room temperature using a Jobin-Yvon HR800 micro-Raman system equipped with a liquid-nitrogen-cooled charge couple detector (CCD), a ×100 objective lens (numerical aperture = 0.90). The excitation energies are 2.54 and 2.71 eV from Ar^+ laser; 1.83, 2.18, 2.34, and 2.41 eV from Kr^+ laser; 1.96 and 2.09 eV from He–Ne laser; and 2.81 eV from He–Cd laser. The 1800 lines/mm grating is used in the Raman measurements, which enables each CCD pixel to cover 0.62 cm^{-1} at 2.54 eV. A typical laser power of 0.3 mW is used to avoid sample heating.

Density Functional Theory Calculation. Density functional theory calculations were performed using the generalized gradient approximation for the exchange–correlation potential, the projector augmented wave method,[69,70] and a plane-wave basis set as implemented in the Vienna ab initio simulation package (VASP).[71] Density functional perturbation theory (DFPT)[58] was employed to calculate phonon-related properties. Vibrational frequencies and amplitudes at the Γ point were calculated using VASP with the DFPT method. The phonon dispersion relations were computed using the Quantum Espresso (QE) code[72] with the ultrasoft pseudopotentials[73,74] for describing ion–electron interactions, while other details are the same as those in the VASP calculations. The kinetic energy cutoff for the plane-wave basis set was 400 eV for all calculations. A k-mesh of $9 \times 9 \times 1$ was adopted to sample the first Brillouin zone of the tBLM with $\theta = 21.79°$ in both geometric optimization and phonon calculations. In structural optimizations, van der Waals interactions were considered under the framework of the vdW-DF method[75,76] with the optB86b exchange functional.[77,78] The vacuum thickness was set large enough (17 Å) in the z-direction to avoid interactions between periodic sheets of tBLMs. The shape (in-plane lattice parameters) of each supercell was fully optimized, and all atoms in the supercell were allowed to relax until the residual force per atom was <0.001 eV/Å. The amplitude distributions of the A_1' and FA_1' modes were interpolated by vibrational amplitudes of sulfur atoms in the two outmost sulfur layers.

ASSOCIATED CONTENT

Ⓢ Supporting Information

Supporting Information is available in the online version of the paper. The Supporting Information is available free of charge on the ACS Publications website at DOI: 10.1021/acsnano.8b05006.

The detailed definitions of moiré superlattice and crystallographic superlattice and the calculated phonon dispersion from interpolation. (PDF)

AUTHOR INFORMATION

Corresponding Author
*E-mail: phtan@semi.ac.cn.

ORCID Ⓞ
Qing-Hai Tan: 0000-0003-4808-4795
Jun Zhang: 0000-0002-9831-6796
Wei Ji: 0000-0001-5249-6624
Ping-An Hu: 0000-0003-3499-2733
Kai-Hui Liu: 0000-0002-8781-2495
Ping-Heng Tan: 0000-0001-6575-1516

Author Contributions
⊥These authors contributed equally to this work

Notes
The authors declare no competing financial interest.

REFERENCES

(1) Liu, Z.; Song, L.; Zhao, S.; Huang, J.; Ma, L.; Zhang, J.; Lou, J.; Ajayan, P. M. Direct Growth of Graphene/Hexagonal Boron Nitride Stacked Layers. *Nano Lett.* **2011**, *11*, 2032−2037.

(2) Gong, Y.; Lin, J.; Wang, X.; Shi, G.; Lei, S.; Lin, Z.; Zou, X.; Ye, G.; Vajtai, R.; Yakobson, B. I.; Terrones, H.; Terrones, M.; Tay, B. K.; Lou, J.; Pantelides, S. T.; Liu, Z.; Zhou, W.; Ajayan, P. M. Vertical and in-Plane Heterostructures from WS_2/MoS_2 Monolayers. *Nat. Mater.* **2014**, *13*, 1135−1142.

(3) Dean, C. R.; Young, A. F.; Meric, I.; Lee, C.; Wang, L.; Sorgenfrei, S.; Watanabe, K.; Taniguchi, T.; Kim, P.; Shepard, K. L.; Hone, J. Boron Nitride Substrates for High-Quality Graphene Electronics. *Nat. Nanotechnol.* **2010**, *5*, 722−726.

(4) Ponomarenko, L. A.; Geim, A. K.; Zhukov, A. A.; Jalil, R.; Morozov, S. V.; Novoselov, K. S.; Grigorieva, I. V.; Hill, E. H.; Cheianov, V. V.; Fal'Ko, V. I.; Watanabe, K.; Taniguchi, T.; Gorbachev, R. V. Tunable Metal-Insulator Transition in Double-Layer Graphene Heterostructures. *Nat. Phys.* **2011**, *7*, 958−961.

(5) Britnell, L.; Gorbachev, R. V.; Jalil, R.; Belle, B. D.; Schedin, F.; Mishchenko, A.; Georgiou, T.; Katsnelson, M. I.; Eaves, L.; Morozov, S. V.; Peres, N. M. R.; Leist, J.; Geim, A. K.; Novoselov, K. S.; Ponomarenko, L. A. Field-Effect Tunneling Transistor Based on Vertical Graphene Heterostructures. *Science* **2012**, *335*, 947−950.

(6) Geim, A. K.; Grigorieva, I. V. Van der Waals Heterostructures. *Nature* **2013**, *499*, 419−425.

(7) Liu, Z.; Ma, L.; Shi, G.; Zhou, W.; Gong, Y.; Lei, S.; Yang, X.; Zhang, J.; Yu, J.; Hackenberg, K. P.; Babakhani, A.; Idrobo, J.-C.; Vajtai, R.; Ajayan, P. M. In-Plane Heterostructures of Graphene and Hexagonal Boron Nitride with Controlled Domain Sizes. *Nat. Nanotechnol.* **2011**, *8*, 119−124.

(8) Li, M.-Y.; Shi, Y.; Cheng, C.-C.; Lu, L.-S.; Lin, Y.-C.; Tang, H.-L.; Tsai, M.-L.; Chu, C.-W.; Wei, K.-H.; He, J.-H.; Chang, W.-H.; Suenaga, K.; Li, L.-J. Epitaxial Growth of a Monolayer WSe_2-MoS_2 Lateral p-n Junction with an Atomically Sharp Interface. *Science* **2015**, *349*, 524−528.

(9) Hunt, B.; Sanchez-Yamagishi, J.; Young, A.; Yankowitz, M.; LeRoy, B. J.; Watanabe, K.; Taniguchi, T.; Moon, P.; Koshino, M.; Jarillo-Herrero, P.; Ashoori, R. C. Massive Dirac Fermions and Hofstadter Butterfly in a van der Waals Heterostructure. *Science* **2013**, *340*, 1427−1430.

(10) Roy, K.; Padmanabhan, M.; Goswami, S.; Sai, T. P.; Ramalingam, G.; Raghavan, S.; Ghosh, A. Graphene-MoS_2 Hybrid Structures for Multifunctional Photoresponsive Memory Devices. *Nat. Nanotechnol.* **2013**, *8*, 826−830.

(11) Schmidt, H.; Rode, J. C.; Smirnov, D.; Haug, R. J. Superlattice Structures in Twisted Bilayers of Folded Graphene. *Nat. Commun.* **2014**, *5*, 5742.

(12) Jiang, T.; Liu, H.; Huang, D.; Zhang, S.; Li, Y.; Gong, X.; Shen, Y.-R.; Liu, W.-T.; Wu, S. Valley and Band Structure Engineering of Folded MoS_2 Bilayers. *Nat. Nanotechnol.* **2014**, *9*, 825−829.

(13) Huang, M.; Li, S.; Zhang, Z.; Xiong, X.; Li, X.; Wu, Y. Multifunctional High-Performance van der Waals Heterostructures. *Nat. Nanotechnol.* **2017**, *12*, 1148−1154.

(14) Calman, E. V.; Fogler, M. M.; Butov, L. V.; Hu, S.; Mishchenko, A.; Geim, A. K. Indirect Excitons in van der Waals Heterostructures at Room Temperature. *Nat. Commun.* **2018**, *9*, 1895.

(15) Rivera, P.; Schaibley, J. R.; Jones, A. M.; Ross, J. S.; Wu, S.; Aivazian, G.; Klement, P.; Seyler, K.; Clark, G.; Ghimire, N. J.; Yan, J.; Mandrus, D. G.; Yao, W.; Xu, X. Observation of Long-Lived Interlayer Excitons in Monolayer MoSe$_2$-WSe$_2$ Heterostructures. *Nat. Commun.* **2015**, *6*, 6242.

(16) Mak, K. F.; Lee, C.; Hone, J.; Shan, J.; Heinz, T. F. Atomically Thin MoS$_2$: a New Direct-Gap Semiconductor. *Phys. Rev. Lett.* **2010**, *105*, 136805.

(17) Zhao, W. J.; Ghorannevis, Z.; Chu, L. Q.; Toh, M. L.; Kloc, C.; Tan, P. H.; Eda, G. Evolution of Electronic Structure in Atomically Thin Sheets of WS$_2$ and WSe$_2$. *ACS Nano* **2013**, *7*, 791−797.

(18) Ci, L.; Song, L.; Jin, C.; Jariwala, D.; Wu, D.; Li, Y.; Srivastava, A.; Wang, Z.; Storr, K.; Balicas, L.; Liu, F.; Ajayan, P. M. Atomic Layers of Hybridized Boron Nitride and Graphene Domains. *Nat. Mater.* **2010**, *9*, 430−435.

(19) Li, G.; Luican, A.; Lopes dos Santos, J. M. B.; Neto, A. C.; Reina, A.; Kong, J.; Andrei, E. Observation of van Hove Singularities in Twisted Graphene Layers. *Nat. Phys.* **2010**, *6*, 109−113.

(20) Bistritzer, R.; MacDonald, A. H. Moiré Bands in Twisted Double-Layer Graphene. *Proc. Natl. Acad. Sci. U. S. A.* **2011**, *108*, 12233−12237.

(21) Xue, J.; Sanchez-Yamagishi, J.; Bulmash, D.; Jacquod, P.; Deshpande, A.; Watanabe, K.; Taniguchi, T.; Jarillo-Herrero, P.; LeRoy, B. J. Scanning Tunnelling Microscopy and Spectroscopy of Ultra-Flat Graphene on Hexagonal Boron Nitride. *Nat. Mater.* **2011**, *10*, 282−285.

(22) Decker, R.; Wang, Y.; Brar, V. W.; Regan, W.; Tsai, H.-Z.; Wu, Q.; Gannett, W.; Zettl, A.; Crommie, M. F. Local Electronic Properties of Graphene on a BN Substrate via Scanning Tunneling Microscopy. *Nano Lett.* **2011**, *11*, 2291−2295.

(23) Woods, C. R.; Britnell, L.; Eckmann, A.; Ma, R. S.; Lu, J. C.; Guo, H. M.; Lin, X.; Yu, G. L.; Cao, Y.; Gorbachev, R. V.; Kretinin, A. V.; Park, J.; Ponomarenko, L. A.; Katsnelson, M. I.; Gornostyrev, Y. N.; Watanabe, K.; Taniguchi, T.; Casiraghi, C.; Gao, H. J.; Geim, A. K.; et al. Commensurate-Incommensurate Transition in Graphene on Hexagonal Boron Nitride. *Nat. Phys.* **2014**, *10*, 451−456.

(24) Dean, C. R.; Wang, L.; Maher, P.; Forsythe, C.; Ghahari, F.; Gao, Y.; Katoch, J.; Ishigami, M.; Moon, P.; Koshino, M.; Taniguchi, T.; Watanabe, K.; Shepard, K. L.; Hone, J.; Kim, P. Hofstadter's Butterfly and the Fractal Quantum Hall Effect in moiré Superlattices. *Nature* **2013**, *497*, 598−602.

(25) Lee, D. S.; Riedl, C.; Beringer, T.; Castro Neto, A. H.; von Klitzing, K.; Starke, U.; Smet, J. H. Quantum Hall Effect in Twisted Bilayer Graphene. *Phys. Rev. Lett.* **2011**, *107*, 216602.

(26) Yankowitz, M.; Xue, J.; Cormode, D.; Sanchez-Yamagishi, J. D.; Watanabe, K.; Taniguchi, T.; Jarillo-Herrero, P.; Jacquod, P.; LeRoy, B. J. Emergence of Superlattice Dirac Points in Graphene on Hexagonal Boron Nitride. *Nat. Phys.* **2012**, *8*, 382−386.

(27) Ponomarenko, L. A.; Gorbachev, R. V.; Yu, G. L.; Elias, D. C.; Jalil, R.; Patel, A. A.; Mishchenko, A.; Mayorov, A. S.; Woods, C. R.; Wallbank, J. R.; Mucha-Kruczynski, B. A.; Piot, M.; Potemski, M.; Grigorieva, I. V.; Novoselov, K. S.; Guinea, F.; Fal'ko, V. I.; Geim, A. K. Cloning of Dirac Fermions in Graphene Superlattices. *Nature* **2013**, *497*, 594−597.

(28) Gorbachev, R. V.; Song, J. C. W.; Yu, G. L.; Kretinin, A. V.; Withers, F.; Cao, Y.; Mishchenko, A.; Grigorieva, I. V.; Novoselov, K. S.; Levitov, L. S.; Geim, A. K. Detecting Topological Currents in Graphene Superlattices. *Science* **2014**, *346*, 448−451.

(29) Yu, H.; Liu, G.-B.; Tang, J.; Xu, X.; Yao, W. Moiré Excitons: from Programmable Quantum Emitter Arrays to Spin-Orbit−Coupled Artificial Lattices. *Sci. Adv.* **2017**, *3*, e1701696.

(30) Carozo, V.; Almeida, C. M.; Ferreira, E. H.; Cançado, L. G.; Achete, C. A.; Jorio, A. Raman Signature of Graphene Superlattices. *Nano Lett.* **2011**, *11*, 4527−4534.

(31) Jorio, A.; Cancado, L. G. Raman Spectroscopy of Twisted Bilayer Graphene. *Solid State Commun.* **2013**, *175*, 3−12.

(32) Eckmann, A.; Park, J.; Yang, H.; Elias, D.; Mayorov, A. S.; Yu, G.; Jalil, R.; Novoselov, K. S.; Gorbachev, R. V.; Lazzeri, M.; Geim, A. K.; Casiraghi, C. Raman Fingerprint of Aligned Graphene/h-BN Super-lattices. *Nano Lett.* **2013**, *13*, 5242−5246.

(33) Liang, L.; Zhang, J.; Sumpter, B. G.; Tan, Q.; Tan, P.-H.; Meunier, V. Low-Frequency Shear and Layer-Breathing Modes in Raman Scattering of Two-Dimensional Materials. *ACS Nano* **2017**, *11*, 11777−11802.

(34) Wu, J.-B.; Lin, M.-L.; Cong, X.; Liu, H.-N.; Tan, P.-H. Raman Spectroscopy of Graphene-Based Materials And Its Applications in Related Devices. *Chem. Soc. Rev.* **2018**, *47*, 1822−1873.

(35) Eliel, G. S. N.; Moutinho, M. V. O.; Gadelha, A. C.; Righi, A.; Campos, L. C.; Ribeiro, H. B.; Chiu, P.-W.; Watanabe, K.; Taniguchi, T.; Puech, P.; Paillet, M.; Michel, T.; Venezuela, P.; Pimenta, M. A. Intralayer and Interlayer Electron-Phonon Interactions in Twisted Graphene Heterostructures. *Nat. Commun.* **2018**, *9*, 1221.

(36) Li, H.; Ying, H.; Chen, X.; Nika, D. L.; Cocemasov, A. I.; Cai, W.; Balandin, A. A.; Chen, S. Thermal Conductivity of Twisted Bilayer Graphene. *Nanoscale* **2014**, *6*, 13402−13408.

(37) Jin, C.; Kim, J.; Suh, J.; Shi, Z.; Chen, B.; Fan, X.; Kam, M.; Watanabe, K.; Taniguchi, T.; Tongay, S.; Zettl, A.; Wu, J.; Wang, F. Interlayer Electron-Phonon Coupling in WSe$_2$/hBN Heterostructures. *Nat. Phys.* **2017**, *13*, 127−131.

(38) Chow, C. M.; Yu, H.; Jones, A. M.; Yan, J.; Mandrus, D. G.; Taniguchi, T.; Watanabe, K.; Yao, W.; Xu, X. Unusual Exciton-Phonon Interactions at van der Waals Engineered Interfaces. *Nano Lett.* **2017**, *17*, 1194−1199.

(39) Wu, J. B.; Zhang, X.; Ijäs, M.; Han, W. P.; Qiao, X. F.; Li, X. L.; Jiang, D. S.; Ferrari, A. C.; Tan, P. H. Resonant Raman Spectroscopy of Twisted Multilayer Graphene. *Nat. Commun.* **2014**, *5*, 5309.

(40) Li, H.; Wu, J.-B.; Ran, F.; Lin, M.-L.; Liu, X.-L.; Zhao, Y.; Lu, X.; Xiong, Q.; Zhang, J.; Huang, W.; Zhang, H.; Tan, P.-H. Interfacial Interactions in van der Waals Heterostructures of MoS$_2$ and Graphene. *ACS Nano* **2017**, *11*, 11714−11723.

(41) Moon, P.; Koshino, M. Optical Absorption in Twisted Bilayer Graphene. *Phys. Rev. B: Condens. Matter Mater. Phys.* **2013**, *87*, 205404.

(42) Holy, J. A.; Klein, M. V.; McMillan, W. L.; Meyer, S. F. Raman-Active Lattice Vibrations of the Commensurate Superlattice in 2H-TaSe$_2$. *Phys. Rev. Lett.* **1976**, *37*, 1145−1148.

(43) Timp, G.; Elman, B.; Al-Jishi, R.; Dresselhaus, G. Observation of Superlattice-Induced Raman Modes in Graphite-Potassium-Amalgam Compounds. *Solid State Commun.* **1982**, *44*, 987−991.

(44) Sood, A. K.; Menendez, J.; Cardona, M.; Ploog, K. Resonance Raman Scattering by Confined LO and TO Phonons in GaAs-AlAs Superlattices. *Phys. Rev. Lett.* **1985**, *54*, 2111−2114.

(45) Tan, P. H.; Bougeard, D.; Abstreiter, G.; Brunner, K. Raman Scattering of Folded Acoustic Phonons in Self-Assembled Si/Ge Dot Superlattices. *Appl. Phys. Lett.* **2004**, *84*, 2632−2634.

(46) Liu, K.; Zhang, L.; Cao, T.; Jin, C.; Qiu, D.; Zhou, Q.; Zettl, A.; Yang, P.; Louie, S. G.; Wang, F. Evolution of Interlayer Coupling in Twisted Molybdenum Disulfide Bilayers. *Nat. Commun.* **2014**, *5*, 4966.

(47) Huang, S.; Liang, L.; Ling, X.; Puretzky, A. A.; Geohegan, D. B.; Sumpter, B. G.; Kong, J.; Meunier, V.; Dresselhaus, M. S. Low-Frequency Interlayer Raman Modes to Probe Interface of Twisted Bilayer MoS$_2$. *Nano Lett.* **2016**, *16*, 1435−1444.

(48) Puretzky, A. A.; Liang, L.; Li, X.; Xiao, K.; Sumpter, B. G.; Meunier, V.; Geohegan, D. B. Twisted MoSe$_2$ Bilayers with Variable Local Stacking and Interlayer Coupling Revealed by Low-Frequency Raman Spectroscopy. *ACS Nano* **2016**, *10*, 2736−2744.

(49) Huang, S.; Ling, X.; Liang, L.; Kong, J.; Terrones, H.; Meunier, V.; Dresselhaus, M. S. Probing the Interlayer Coupling of Twisted Bilayer MoS$_2$ Using Photoluminescence Spectroscopy. *Nano Lett.* **2014**, *14*, 5500−5508.

(50) Lui, C. H.; Ye, Z. P.; Ji, C.; Chiu, K. C.; Chou, C. T.; Andersen, T. I.; Means-Shively, C.; Anderson, H.; Wu, J. M.; Kidd, T.; Lee, Y. H.; He, R. Observation of Interlayer Phonon Modes in van der Waals

Heterostructures. *Phys. Rev. B: Condens. Matter Mater. Phys.* **2015**, *91*, 165403.

(51) Lauritsen, J. V.; Kibsgaard, J.; Helveg, S.; Topsøe, H.; Clausen, B. S.; Laegsgaard, E.; Besenbacher, F. Size-Dependent Structure of MoS_2 Nanocrystals. *Nat. Nanotechnol.* **2007**, *2*, 53−58.

(52) van der Zande, A. M.; Huang, P. Y.; Chenet, D. A.; Berkelbach, T. C.; You, Y.; Lee, G.-H.; Heinz, T. F.; Reichman, D. R.; Muller, D. A.; Hone, J. C. Grains and Grain Boundaries in Highly Crystalline Monolayer Molybdenum Disulphide. *Nat. Mater.* **2013**, *12*, 554−561.

(53) Cheng, J.; Jiang, T.; Ji, Q.; Zhang, Y.; Li, Z.; Shan, Y.; Zhang, Y.; Gong, X.; Liu, W.; Wu, S. Kinetic Nature of Grain Boundary Formation in As-Grown MoS_2 Monolayers. *Adv. Mater.* **2015**, *27*, 4069−4074.

(54) Wu, J. B.; Zhao, H.; Li, Y.; Ohlberg, D.; Shi, W.; Wu, W.; Wang, H.; Tan, P. H. Monolayer Molybdenum Disulfide Nanoribbons with High Optical Anisotropy. *Adv. Opt. Mater.* **2016**, *4*, 756−762.

(55) Zhang, X.; Qiao, X.-F.; Shi, W.; Wu, J.-B.; Jiang, D.-S.; Tan, P.-H. Phonon and Raman Scattering of Two-Dimensional Transition Metal Dichalcogenides from Monolayer, Multilayer to Bulk Material. *Chem. Soc. Rev.* **2015**, *44*, 2757−2785.

(56) Molina-Sanchez, A.; Wirtz, L. Phonons in Single-Layer and Few-Layer MoS_2 and WS_2. *Phys. Rev. B: Condens. Matter Mater. Phys.* **2011**, *84*, 155413.

(57) Zhang, X.; Han, W. P.; Wu, J. B.; Milana, S.; Lu, Y.; Li, Q. Q.; Ferrari, A. C.; Tan, P. H. Raman Spectroscopy of Shear and Layer Breathing Modes in Multilayer MoS_2. *Phys. Rev. B: Condens. Matter Mater. Phys.* **2013**, *87*, 115413.

(58) Baroni, S.; de Gironcoli, S.; Dal Corso, A.; Giannozzi, P. Phonons and Related Crystal Properties from Density-Functional Perturbation Theory. *Rev. Mod. Phys.* **2001**, *73*, 515−562.

(59) Campos Delgado, J.; Cançado, L. G.; Achete, C. A.; Jorio, A.; Raskin, J. P. Raman Scattering Study of the Phonon Dispersion in Twisted Bilayer Graphene. *Nano Res.* **2013**, *6*, 269−274.

(60) Wang, Y.; Su, Z.; Wu, W.; Nie, S.; Xie, N.; Gong, H.; Guo, Y.; Hwan Lee, J.; Xing, S.; Lu, X.; Wang, H.; Lu, X.; McCarty, K.; Pei, S.-s.; Robles-Hernandez, F.; Hadjiev, V. G.; Bao, J. Resonance Raman Spectroscopy of G-Line and Folded Phonons in Twisted Bilayer Graphene with Large Rotation Angles. *Appl. Phys. Lett.* **2013**, *103*, 123101.

(61) He, R.; Chung, T.-F.; Delaney, C.; Keiser, C.; Jauregui, L. A.; Shand, P. M.; Chancey, C. C.; Wang, Y.; Bao, J.; Chen, Y. P. Observation of Low Energy Raman Modes in Twisted Bilayer Graphene. *Nano Lett.* **2013**, *13*, 3594−3601.

(62) Righi, A.; Venezuela, P.; Chacham, H.; Costa, S.; Fantini, C.; Ruoff, R.; Colombo, L.; Bacsa, W.; Pimenta, M. Resonance Raman Spectroscopy in Twisted Bilayer Graphene. *Solid State Commun.* **2013**, *175*, 13−17.

(63) Carozo, V.; Almeida, C. M.; Fragneaud, B.; Bedê, P. M.; Moutinho, M. V. O.; Ribeiro-Soares, J.; Andrade, N. F.; Souza Filho, A. G.; Matos, M. J. S.; Wang, B.; Terrones, M.; Capaz, R. B.; Jorio, A.; Achete, C. A.; Cançado, L. G. Resonance Effects on the Raman Spectra of Graphene Superlattices. *Phys. Rev. B: Condens. Matter Mater. Phys.* **2013**, *88*, 085401.

(64) Qiu, D. Y.; da Jornada, F. H.; Louie, S. G. Optical Spectrum of MoS_2: Many-Body Effects and Diversity of Exciton States. *Phys. Rev. Lett.* **2013**, *111*, 216805.

(65) Carvalho, B. R.; Malard, L. M.; Alves, J. M.; Fantini, C.; Pimenta, M. A. Symmetry-Dependent Exciton-Phonon Coupling in 2D and Bulk MoS_2 Observed by Resonance Raman Scattering. *Phys. Rev. Lett.* **2015**, *114*, 136403.

(66) Lee, J.-U.; Park, J.; Son, Y.-W.; Cheong, H. Anomalous Excitonic Resonance Raman Effects in Few-Layered MoS_2. *Nanoscale* **2015**, *7*, 3229−3236.

(67) Kim, S.; Kim, K.; Lee, J.-U.; Cheong, H. Excitonic Resonance Effects and Davydov Splitting in Circularly Polarized Raman Spectra of Few-Layer WSe_2. *2D Mater.* **2017**, *4*, 045002.

(68) Wu, J. B.; Hu, Z. X.; Zhang, X.; Han, W. P.; Lu, Y.; Shi, W.; Qiao, X. F.; Ijiäs, M.; Milana, S.; Ji, W.; Ferrari, A. C.; Tan, P. H. Interface Coupling in Twisted Multilayer Graphene by Resonant Raman Spectroscopy of Layer Breathing Modes. *ACS Nano* **2015**, *9*, 7440−7449.

(69) Blochl, P. E. Projector Augmented-Wave Method. *Phys. Rev. B: Condens. Matter Mater. Phys.* **1994**, *50*, 17953.

(70) Kresse, G.; Joubert, D. From Ultrasoft Pseudopotentials to the Projector Augmented-Wave Method. *Phys. Rev. B: Condens. Matter Mater. Phys.* **1999**, *59*, 1758.

(71) Kresse, G.; Furthmuller, J. Efficient Iterative Schemes for *ab initio* Total-Energy Calculations using a Plane-Wave Basis Set. *Phys. Rev. B: Condens. Matter Mater. Phys.* **1996**, *54*, 11169.

(72) Giannozzi, P.; Baroni, S.; Bonini, N.; Calandra, M.; Car, R.; Cavazzoni, C.; Ceresoli, D.; Chiarotti, G. L.; Cococcioni, M.; Dabo, I.; Dal Corso, A.; de Gironcoli, S.; Fabris, S.; Fratesi, G.; Gebauer, R.; Gerstmann, U.; Gougoussis, C.; Kokalj, A.; Lazzeri, M.; Martin-Samos, L.; et al. QUANTUM ESPRESSO: a Modular and Open-Source Software Project for Quantum Simulations of Materials. *J. Phys.: Condens. Matter* **2009**, *21*, 395502.

(73) Vanderbilt, D. Soft Self-Consistent Pseudopotentials in a Generalized Eigenvalue Formalism. *Phys. Rev. B: Condens. Matter Mater. Phys.* **1990**, *41*, 7892−7895.

(74) Rappe, A. M.; Rabe, K. M.; Kaxiras, E.; Joannopoulos, J. D. Optimized Pseudopotentials. *Phys. Rev. B: Condens. Matter Mater. Phys.* **1990**, *41*, 1227−1230.

(75) Dion, M.; Rydberg, H.; Schröder, E.; Langreth, D. C.; Lundqvist, B. I. Van der Waals Density Functional for General Geometries. *Phys. Rev. Lett.* **2004**, *92*, 246401.

(76) Lee, K.; Murray, E. D.; Kong, L.; Lundqvist, B. I.; Langreth, D. C. Higher-Accuracy van der Waals Density Functional. *Phys. Rev. B: Condens. Matter Mater. Phys.* **2010**, *82*, 081101.

(77) Klimeš, J.; Bowler, D. R.; Michaelides, A. Van der Waals Density Functionals Applied to Solids. *Phys. Rev. B: Condens. Matter Mater. Phys.* **2011**, *83*, 195131.

(78) Klimeš, J.; Bowler, D. R.; Michaelides, A. Chemical Accuracy for the van der Waals Density Functional. *J. Phys.: Condens. Matter* **2010**, *22*, 022201.